Phase diagram for injection locking a superradiant laser

Kevin C. Cox, Joshua M. Weiner, and James K. Thompson

JILA, NIST, and Department of Physics, University of Colorado, Boulder, Colorado 80309-0440, USA

We study experimentally and theoretically the response of a superradiant or bad-cavity laser to an applied coherent drive. We observe two forms of synchronization (injection locking) between the superradiant ensemble and the applied drive: one attractive and one repulsive in nature. In the region of repulsion, the atomic spin state that stores laser coherence undergoes three-dimensional dynamics, as opposed to a two-parameter description of the electric field in a traditional good-cavity laser. We derive a phase diagram of predicted behavior and experimentally measure the response of the system across various trajectories therein.

In a superradiant (or "bad-cavity") laser, the atomic coherence decays much more slowly than the optical cavity field. As such, the atomic coherence primarily stores the laser's phase information and is initially established via spontaneous synchronization of the individual atomic dipoles [as in Fig. 1(a)]. Unlike in conventional good-cavity lasers, coherence has been shown to persist with less than one, and even zero, intracavity photons [1–3]. This bad-cavity regime of laser physics has generated recent interest because it offers a promising route for overcoming fundamental thermal mirror noise in order to realize laser linewidths of 1 mHz or less [4].

More broadly, cold-atom–cavity systems are extremely well-controlled experiments useful for observing many-body phenomena with the cavity mode providing strong long-range interactions between the atoms. For example, the spontaneous spatial ordering [5–8] and realization of the Dicke model [9] in cold-atom–cavity systems are examples of nonequilibrium phase transitions and provide insight into our fundamental understanding of phase transitions in condensed-matter physics [10]. Further, atomic ensembles coupled to many cavity modes may allow the creation of exotic phases of matter with emergent crystallization and frustration [11,12], and they could serve as a model system for associative memories [13]. Superradiant lasers have been identified as an interesting system in which to study the problem of synchronization of quantum oscillators [14–16]. In all, superradiant atom-cavity systems and related systems promise continuing interest for both technological and fundamental reasons.

In this paper, we study the synchronization of a cold-atom-based superradiant laser to an externally applied optical field that is injected into the lasing cavity mode [Fig. 1(a)]. The synchronization is analogous to injection locking in a good-cavity laser, but in this superradiant system phase locking is manifested as collective synchronization of an ensemble of cold atoms to the applied drive. For a weak applied drive, the system can be approximately mapped to a driven Van der Pol self-oscillator, a canonical system in synchronization physics [18,19]. We directly observe the two synchronization behaviors predicted for such a system. However, when the applied drive or detuning of the drive are large, we observe two additional effects that are not explained by either the Van der Pol model or traditional injection locking theory [20]. First, the stimulated emission component at the self-lasing frequency is repulsed from, rather than attracted to, the drive frequency.

Second, as the drive strength is increased, the stimulated output power at the drive frequency actually decreases. These two effects arise from the full three-dimensional (3D) description of the atomic spin or Bloch vector dynamics, in comparison with a two-dimensional description of a Van der Pol oscillator. The third degree of freedom corresponds to the atomic inversion, which is no longer approximately constant at large detunings or drive strengths. In each regime, we show good quantitative understanding of our system, providing a solid foundation for future work in fundamental physics using superradiant lasers.

Complex injection locking behaviors beyond the simple Van der Pol description, including instability, chaos, and repulsion, have been theoretically studied and observed in lasers that operate in the crossover regime of laser physics where the cavity decay rate and one or more atomic decay rates are similar [21–23]. Frequency repulsion is predicted in these lasers from a coupling between the injection locking dynamics and relaxation oscillations [24]. In a distributed feedback (DFB) laser, a one-sided frequency repulsion was seen to arise from tuning of the cavity frequency [25]. In our system, frequency repulsion and three-dimensional dynamics are a direct consequence of injection locking deep in the bad-cavity regime, a regime largely inaccessible by previous work [26].

The apparatus for the superradiant laser and principles behind its basic operation have been described in detail in previous work [1–3,17]. The atomic gain medium consists of $N \approx 1.1 \times 10^6$ ^{87}Rb atoms cooled to 10–20 μK and trapped in a 1D optical lattice inside of an optical cavity with power decay linewidth $\kappa = 2\pi \times 11.8$ MHz. The atoms are tightly confined to $\ll \lambda$ (i.e., the Lamb-Dicke regime) along the cavity axis, but only weakly confined perpendicular to the cavity axis.

A dressing laser is applied transverse to the cavity to induce spontaneous Raman transitions between two hyperfine ground states $|\uparrow\rangle \equiv |5S_{1/2}, F = 2, m_F = 0\rangle$ to $|\downarrow\rangle \equiv |5S_{1/2}, F = 1, m_F = 0\rangle$, with typical single-atom free-space Raman transition rates $\gamma = 2\pi \times 100$ Hz to $2\pi \times 300$ Hz. The cavity frequency ω_c is tuned to be on or near resonance with the spontaneously emitted light's frequency ω_a. The effective two-photon coupling to the cavity is characterized by the rms value of the Jaynes-Cummings coupling constant g_2 [27] and single-atom cooperativity parameter $C = \frac{4g_2^2}{\kappa\gamma} = 5 \times 10^{-3}$.
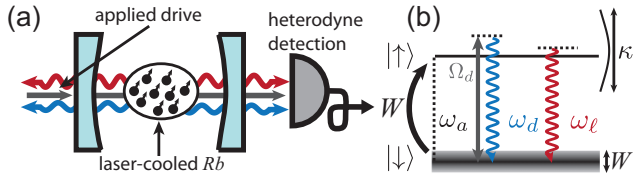
FIG. 1. (Color online) Experimental setup and level diagram. (a) Atoms interact with both the externally applied drive (gray) and the intracavity field generated by their collective emission (blue and red). The superradiant laser responds primarily at two frequencies, the drive frequency ω_d and a self-lasing frequency ω_ℓ. (b) The characteristic frequencies are displayed in a level diagram, and all lie within one cavity mode of width κ. The Raman laser system is approximated as a two-level laser incoherently repumped through intermediate optically excited states (not shown) at rate W. W is also the primary source of broadening of the lasing transition (shown as broadening of $|\downarrow\rangle$). In this work, the ratio of atomic and optical linewidths is $W/\kappa \approx 5 \times 10^{-2}$ to $5 \times 10^{-3} \ll 1$, placing the system deep into the bad-cavity or superradiant regime. The state $|\uparrow\rangle$ is a dressed state consisting of a ground hyperfine state of Rb coupled nonresonantly to an optically excited state as described in [1–3,17]. The applied drive couples $|\downarrow\rangle$ and $|\uparrow\rangle$ with an on-resonance Rabi frequency Ω_d.

The collective (or superradiant) emission rate for a single atom scales as $NC\gamma$.

To maintain population inversion and steady-state emission, additional lasers are applied to incoherently repump atoms through optically excited states from $|\downarrow\rangle$ back to $|\uparrow\rangle$. The characteristic repumping rate from $|\downarrow\rangle$ (including Rayleigh scattering) is $W \approx 2\pi \times 60$ kHz to $2\pi \times 500$ kHz. The repumping process is the primary contribution to the atomic transverse decoherence rate $\gamma_\perp \approx W/2 + \Gamma_D$. We measure a small additional contribution to the transverse broadening Γ_D that is primarily due to Doppler broadening of the two-photon transition from $|\uparrow\rangle$ to $|\downarrow\rangle$ resulting from the weak transverse confinement of the atoms.

A conceptually simplified experimental diagram for this work is shown in Fig. 1. The key distinct feature in this work is the application of an additional coherent drive to the superradiant laser's cavity mode (Fig. 1). The drive couples the upper $|\uparrow\rangle$ and lower $|\downarrow\rangle$ lasing states with a single-atom Rabi frequency Ω_d. The drive frequency ω_d is detuned from the effective atomic transition frequency ω_a by $\delta_d \equiv \omega_d - \omega_a$ [Fig. 1(b)]. The behavior of the system depends on the relative magnitudes of drive strength Ω_d, detuning δ_d, and characteristic rates of the superradiant laser: the repumping rate W and characteristic collective emission rate into the cavity $NC\gamma$ given by the collective cooperativity NC and the single-atom decay rate γ from $|\uparrow\rangle$ to $|\downarrow\rangle$.

When no drive is applied, the laser emits at frequency ω_{ℓ_0} near, but not necessarily identical to, ω_a. When the drive is applied, the lasing frequency ω_ℓ is shifted by the atoms' interaction with the drive by $\delta_\ell \equiv \omega_\ell - \omega_{\ell_0}$. Additionally, the laser can emit at the drive frequency ω_d. We detect the light emitted from the cavity using heterodyne detection. This gives complete information about the emission spectrum and allows us to measure ω_ℓ, ω_d, and the phases and amplitudes of the electric fields emitted from the cavity at these frequencies. Other frequency components in the laser emission
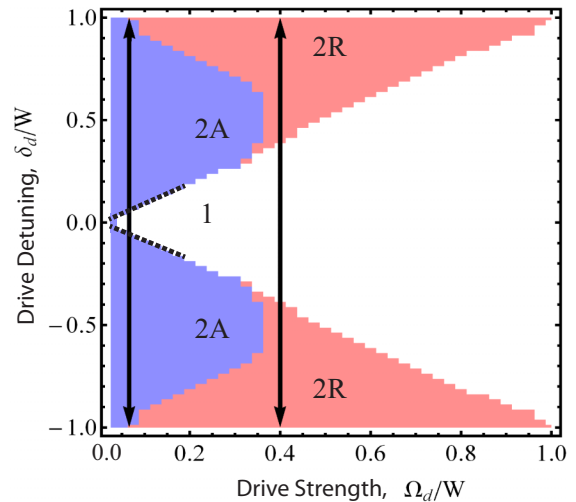

FIG. 2. (Color online) The predicted phase diagram for the driven superradiant laser is shown in a plane defined by the applied drive strength Ω_d and the drive detuning δ_d, normalized to the repumping rate W, which is fixed to $NC\gamma/2$ here. The regions are first divided by the number of distinct emission frequencies [(1) or (2)]. Region (2) is further divided by the frequency shift of the self-lasing component at ω_ℓ, which can be attracted (2A) or repelled (2R) from the applied drive frequency ω_d. When $\Omega_d < 0.2 \times W$, the laser synchronizes by smoothly coalescing in frequency with the drive (dashed line). For larger drives, the self-lasing component remains distinct and is quenched. The two trajectories (black arrows) refer to the two parameter trajectories explored by the data in Fig. 3.

are expected and observed at sums and differences of ω_ℓ and ω_d. These additional components can become rather large near synchronization (see Ref. [18]), but detailed treatment is beyond the scope of this work.

The predicted behavior of the emitted field of the laser is summarized by the theoretical phase diagram in Fig. 2. The phase diagram is calculated by numerically integrating optical Bloch equations based on a simplified two-level model for the superradiant laser (see [28] and Appendix A). For simplification, the repumping rate W is set to a value that optimizes the output power of the laser, $W_{\text{opt}} = \frac{1}{2}NC\gamma$ [4], so that the characteristic rates governing the phase diagram are the two ratios Ω_d/W and δ_d/W.

The primary feature of the phase diagram is the synchronization or nonsynchronization of the superradiant emission to the drive. In the unsynchronized phase of region (2), the atomic dipoles are not perfectly synchronized to the drive and the spectrum of light contains two distinct frequency components at the drive frequency ω_d and the self-lasing frequency ω_ℓ. In contrast in region (1), the atomic dipoles become synchronized to the drive and all light emission occurs at ω_d. For the optimum repumping $W = W_{\text{opt}}$ here, the synchronization transition occurs roughly when $\Omega_d = \delta_d$.

The unsynchronized region (2) is broken into two subregions, delineated by the self-lasing's attraction toward or repulsion from the drive frequency. The region of attraction ($\frac{\delta_\ell}{\delta_d} > 0$) is labeled (2A) in the phase diagram. The region of repulsion ($\frac{\delta_\ell}{\delta_d} < 0$) is labeled (2R). As δ_d or Ω_d are tuned, the behavior of the approach to synchronization depends on

whether one enters region (1) from region (2A) or (2R). For attractive synchronization [from (2A) to (1)], as the $\Omega_d = \delta_d$ boundary is crossed, ω_ℓ is pulled toward the drive. For drive strengths $\Omega_d < 0.2 \times W$ (dashed line in Fig. 2), the self-lasing component synchronizes by smoothly coalescing with the drive at ω_d. When $\Omega_d > 0.2 \times W$, the self-lasing is driven to zero before coalescence can occur. In the repulsive synchronization [from (2R) to (1) in the phase diagram], as one approaches synchronization, ω_ℓ is repelled in frequency from ω_d and the self-lasing component is driven to zero so that the superradiant ensemble is emitting power only at the drive frequency ω_d.

In the limit $\Omega_d, |\delta_d| \ll W$, the laser inversion J_z is approximately fixed, and the three-dimensional Bloch vector (J_x, J_y, J_z) describing the atomic ensemble can be reduced to an effective two-dimensional object described by the transverse coherence $J_- = J_x - iJ_y$. In this case, the equation describing the time evolution of J_- is closely equivalent to that of a driven Van der Pol oscillator, for which attractive synchronization [(2A) to (1)] with and without coalescence (characterized by saddle-node and Hopf bifurcations, respectively) has been well studied [18,19]. We outline this mapping explicitly in Appendix C.

However, when either Ω_d or $|\delta_d| \gtrsim W$, the inversion J_z can no longer be approximated as fixed and the dynamic response of the full three-dimensional Bloch vector must be considered. The response of the extra degree of freedom J_z leads to the repulsive behavior in region (2R), which can be interpreted as an ac Stark shift (Appendix C).

Experimental examples of the two synchronization transitions are shown in Fig. 3, with approximate trajectories in the phase diagram represented by black arrows in Fig. 2. Figure 3(a) demonstrates attractive, coalescing synchronization, and Fig. 3(b) represents repulsive synchronization. The left plots are two-dimensional power spectra of the laser emission. Each horizontal slice corresponds to a single power spectrum of laser emission where color represents the optical power in each frequency bin. The nominal detuning δ_d is changed between experimental trials and plotted on the left axis. On the horizontal axis, the drive frequency ω_d is set to zero so that in the absence of an applied drive ($\Omega_d = 0$), the emission frequency ω_ℓ would follow the diagonal red line. At sufficiently small detunings, synchronization occurs and only power at ω_d is observed. A faint spectral component in Fig. 3 appears on the opposite side of zero from the self-lasing component. We believe this small feature is an artifact of nonlinearities in the detection system.

The spectrograms illustrate the qualitative differences between the two types of synchronization. In Fig. 3(a), the self-lasing frequency ω_ℓ is attracted toward and joins ω_d as $|\delta_d|$ becomes small. In Fig. 3(b), the two emission components remain distinct until the ω_ℓ component is extinguished. To more clearly illustrate the attraction and repulsion, the measured quantity $\delta_\ell = \omega_\ell - \omega_{\ell_0}$ is plotted on the right. The plots are overlaid with color and labeled to help identify the repulsion (red) and attraction regions (blue) matching the phase diagram of Fig. 2. For the trajectory at small Ω_d, the laser goes from synchronized (1), to attraction (2A), to repulsion (2R), as predicted. For the trajectory at larger ω_d, there is a single transition from (1)- to (2R)-like responses. Both behaviors
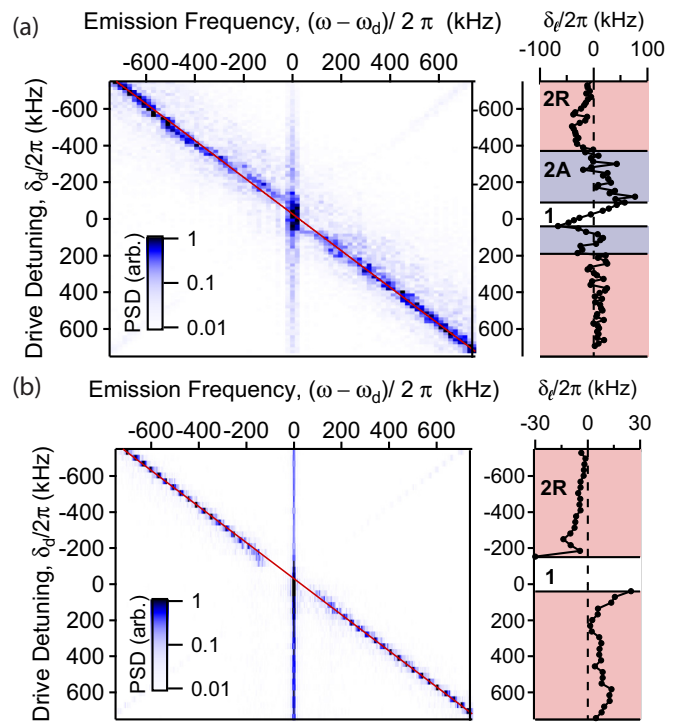

FIG. 3. (Color online) Experimental observation of coalescing attractive (a) and repulsive (b) synchronizations. (Left) 2D spectrograms are taken with fixed drive strength Ω_d as the detuning of the drive δ_d is varied along the representative vertical trajectories in Fig. 2. Darker colors indicate higher power in a frequency bin (i.e., PSD). The red line indicates the expected self-lasing trajectory in the absence of an applied drive. (Right) Two panels show the frequency shift $\delta_\ell = \omega_\ell - \omega_{\ell_0}$ between the lasing frequency and the lasing frequency when no drive is present. In each region, we qualitatively identify attraction and repulsion by the sign of δ_ℓ and label and color each region similarly to the phase diagram in Fig. 2. The behaviors follow the prediction for their respective trajectories across the phase diagram, which are represented by vertical lines in Fig. 2.

qualitatively agree with the prediction from the phase diagram for a two-level laser, shown by the trajectories in Fig. 2.

The qualitative behavior of the data exhibits asymmetry with respect to $\delta_d = 0$, whereas the theoretical phase diagram of Fig. 2 is symmetric. This is because the data did not strictly follow the vertical trajectories shown in Fig. 2. As the detuning δ_d was changed, the fractional amount of the fixed incident drive power coupled into the cavity changed, following the Lorentzian cavity resonance profile. The symmetry of this effect about $\delta_d = 0$ is broken by the fact that $\delta_c \equiv \omega_c - \omega_a \neq 0$ (where ω_c is the cavity resonance frequency), leading to the observed asymmetry in the data of Fig. 3.

We now turn to the development of a perturbative description of the system far from synchronization and the break down of this description as the system approaches and ultimately crosses the synchronization threshold. Deep into region (2) of the phase diagram, the superradiant laser's response to the drive is small and can be understood as a small modulation of the initially undriven Bloch vector describing the atomic coherence. The modulated Bloch vector then radiates an additional field into the cavity at the drive frequency ω_d,
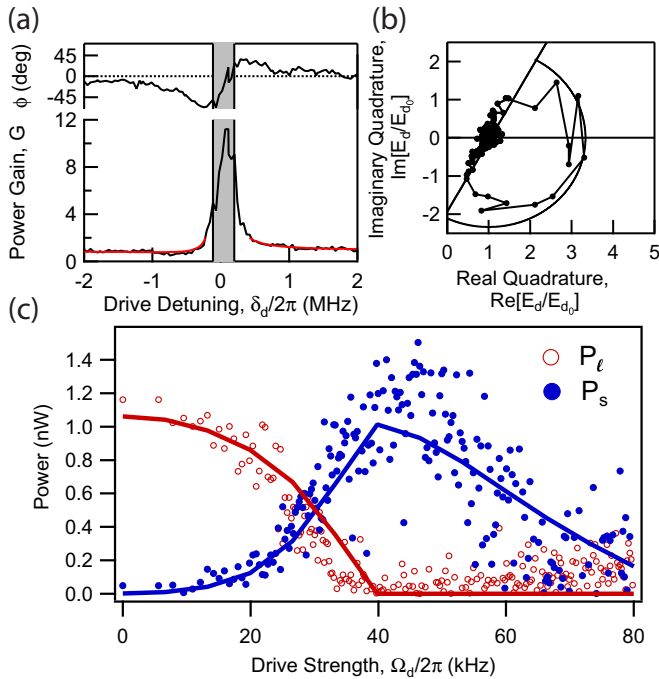
FIG. 4. (Color online) Synchronization and gain saturation. (a) Measured gain and phase response of the superradiant laser at the drive frequency ω_d. At large drive detunings, the response displays linear small-signal gain (red fit to perturbative model overlayed). The gain saturates (gray shaded region) at small detunings as the laser approaches the synchronization transition. (b) The same gain and phase response are represented in a phasor picture. Points of small signal gain lie along the straight line, and the region of saturation is approximately described by a curve of maximum stimulated electric field (inner curve). (c) The stimulated output powers P_s and P_ℓ, at the self-lasing frequency ω_ℓ (red) and at the drive frequency ω_d (blue), respectively, are displayed as the laser is driven across a repulsive synchronization transition at approximately $\Omega_d/2\pi \approx 40$ kHz. Theoretical predictions (solid lines) show good agreement with the data.

producing gain. In Fig. 4(a), we measure this power gain G and phase response ϕ of the laser at the drive frequency ω_d versus the drive detuning δ_d. This corresponds to a vertical trajectory on the phase diagram where, in this dataset, $\frac{\Omega_d}{W} \approx 0.04$. A fit to a perturbative model based on the optical Bloch equations in Appendix B is shown in red.

At small detunings (gray region), the gain and phase response begin to saturate, and deviate from the predicted small-signal values. This is roughly the point when the laser begins to synchronize to the drive and the emission at frequencies other than ω_d begin to disappear. In Fig. 4(a), we have chosen a specific drive strength ($\frac{\Omega_d}{W} \approx 0.04$) to illustrate the transition from linear gain to saturation. If a smaller (larger) drive strength is chosen, we observe that, as expected, saturation occurs at a smaller (larger) detuning.

In Fig. 4(b), the equivalent complex electric field response E_d at the drive frequency is shown in a phasor diagram with each point corresponding to the measured field at a given detuning in Fig. 4(a). The drive response when no atoms are present E_{d_0} is normalized to be real and of length 1. In

the perturbative limit, the additional stimulated field follows a straight line. The line of small-signal gain is tilted due to an additional phase shift of the stimulated field arising from nonzero detuning of the drive from the optical cavity, $\omega_d - \omega_c \neq 0$. At saturation, the stimulated field deviates from the straight line and qualitatively follows a contour of constant stimulated electric field (solid semicircle).

In Fig. 4(c), we show an example of how optical power is "stolen" from the self-lasing frequency ω_ℓ and transferred to the drive frequency. Here the drive strength Ω_d is increased at a fixed detuning $\delta_d/W = 2.2$, and the vertical axis shows the self-lasing power P_ℓ and the stimulated drive power $P_s \equiv P_d - P_{d_0}$. P_{d_0} is the detected power at the drive frequency in the absence of any atomic response, scaling as $P_{d_0} \propto \Omega_d^2$, such that P_s represents the extra stimulated power at ω_d. This dataset corresponds to tuning the system along a horizontal line in Fig. 2 that lies outside the plotted range and such that the system crosses from the repulsive region (2R) to the synchronized region (1).

Numerical solutions [solid lines in Fig. 4(c)] of the optical Bloch equations (Appendix A l) give reasonable agreement with the data. The theoretical model includes approximate corrections for an additional cavity tuning effect [2], and the absolute vertical scale of the theory has been scaled so that the P_ℓ agrees with the data at $\Omega_d = 0$.

The synchronization point in these data is represented by the sharp point when P_ℓ hits zero, with a discontinuous first derivative in P_ℓ and P_s. At the synchronization point, P_s is approximately the original output power of the laser when Ω_d is zero. At large drive strengths in Fig. 4(c), Ω_d becomes much larger than W and the total output power of the laser decreases due to repumping-induced dephasing of the rapid Rabi oscillations caused by the drive. This reduction in stimulated output power is another unique aspect to injection locking in the bad cavity laser.

We have observed two different types of synchronization transitions of a superradiant laser to an external drive, one attractive and one repulsive in nature. The synchronization transition is analogous to a ferromagnet in the presence of an applied magnetic field, the drive breaking a continuous symmetry of the laser with respect to phase [29]. However, the laser steady state is far from thermodynamic equilibrium, making our well-controlled cold-atom–cavity system an interesting avenue for continued study of nonequilibrium phase transitions with modern approaches [10].

It is often useful to apply an external drive to a superradiant laser. Such drives have been used, for instance, to probe the frequency of the optical cavity in Raman-laser systems such as ours (as was done in Ref. [17]) or perhaps in future narrow linewidth superradiant lasers to reduce errors, inaccuracies, and technical noise due to cavity frequency pulling. This work establishes an understanding of how such a technical probe will affect the system. Furthermore, the phase response within the saturation region of Fig. 4(a) could be used as an error signal for a form of active spectroscopy of the gain medium, in some sense the inverse approach to that of Ref. [30], although the fundamental signal-to-noise of such an approach is an open question.

In the future, this work will guide the interpretation of other proposed experiments in cold-atom–cavity systems.

For instance, multiple superradiant subensembles each with an independent transition frequency ω_a can be engineered to interact with each other through one or multiple cavity modes [11–16]. Furthermore, while injection locking is well-described by a mean-field description, and therefore can be considered classical behavior, recent theoretical works propose systems of multiple superradiant ensembles where quantum noise becomes observably large and may serve to drive the phase transitions and affect the average behavior [14–16].

APPENDIX A: OPTICAL BLOCH EQUATIONS

The average behavior of the superradiant laser with an applied drive can be understood with slight modifications to the optical Bloch equations presented in [28]. The optical Bloch equations describe the time evolution of expectation values of the cavity annihilation operator $\hat{a}$ and the collective atomic operators, $\hat{J}_z$ and $\hat{J}_-$, defined as

$$\hat{J}_z = \sum_{i=1}^{N} \frac{|\uparrow_i\rangle\langle\uparrow_i| - |\downarrow_i\rangle\langle\downarrow_i|}{2}, \tag{A1}$$

$$\hat{J}_- = \sum_{i=1}^{N} |\downarrow_i\rangle\langle\uparrow_i|. \tag{A2}$$

$\hat{J}_z$ and $\hat{J}_-$ represent the atomic inversion and transverse coherence, respectively. The optical Bloch equations govern the time evolution of the expectation values of these operators, $J_z = \langle\hat{J}_z\rangle$, $J_- = \langle\hat{J}_-\rangle$, and $E = \langle\hat{a}\rangle$. The atomic response can be visualized as a three-dimensional Bloch vector with x and y projections of the vector given by $J_- = (J_x - iJ_y)/2$. E is a complex representation of the optical cavity electric field such that $|E|^2$ is the average number of photons inside the cavity. The nonlinear equations are closed by approximating that the expectation values of products of operators can be factorized into products of expectation values. Assuming uniform coupling to the cavity mode, the coupled equations for a two-level system with an applied drive can be written as

$$\dot{E} = -\left(\frac{\kappa}{2} + i\delta_c\right)E - ig_2 J_- + \frac{\kappa}{2}E_{d_i}e^{i\delta_d t}, \tag{A3}$$

$$\dot{J}_- = -\gamma_\perp J_- + i2g_2 J_z E, \tag{A4}$$

$$\dot{J}_z = -WJ_z + \frac{N}{2}W + ig_2(J_- E^* - J_-^* E). \tag{A5}$$

The equations are written in a frame rotating at the atom's natural transition frequency ω_a. E_{d_i} is proportional to the amplitude of the electric field of the applied drive incident on the optical cavity. $\delta_c = \omega_c - \omega_a$ is the detuning of the cavity

from the natural atomic transition frequency ω_a. The rest of the equation parameters are defined in the previous text. The Rabi frequency of the drive is related to these parameters by $\Omega_d = \frac{2g_2 E_{d_i}}{1+\tilde{\delta}_c^2}$, where quantities $\tilde{A} \equiv \frac{A}{\kappa/2}$. The measured intracavity field when no atoms are present is $E_{d_0} = \frac{E_{d_i}}{1+i\tilde{\delta}_{d,c}}$, where $\delta_{d,c}$ is the detuning of the driving electric field from the cavity resonance, $\delta_{d,c} = \omega_d - \omega_c$.

We have numerically solved these equations to derive the phase diagram of Fig. 2 and to create theoretical curves for Fig. 4. The two-level model does a reasonable job of predicting the behavior of synchronization versus Ω_d and δ_d. However, due to the true multilevel structure of the laser, these equations cannot be used to predict the total output power of the system. When these equations are not adequate, multilevel optical Bloch equations from Ref. [28] can be used. Additionally, to approximately account for dispersive shifts of the optical cavity in our Raman laser, the cavity detuning δ_c is made a function of J_z to generate the theory for Fig. 4(c). Details can be found in Ref. [28].

APPENDIX B: DERIVATION OF SMALL-SIGNAL GAIN

The small-signal regions of gain and phase response, as described in the main text, follow a simple form that can be derived from the optical Bloch equations. We first assume κ is larger than all other characteristic frequencies in the system so that E adiabatically follows J_-. We then assume that J_- primarily responds at two frequencies, ω_a and ω_d, and we make the ansatz $J_- = J_{-a} + J_{-d}e^{i\delta_d t}$. Lastly, we assume that in this perturbative limit, J_z is unaffected by the weak drive and retains its steady-state value with no drive, $J_{z_{ss}} = \frac{W(1+\tilde{\delta}_c^2)}{2C\gamma}$. With these approximations, we find the small-signal complex field response at the drive frequency. The total detected field at the drive frequency, $E_d = E_{d_0} + E_s$, has two contributions. One contribution (E_{d_0}) comes from the drive alone, and the other (E_s) from atomic stimulation. The small-signal form of E_s is given by

$$E_s = \frac{-iE_{d_0}\gamma_\perp\left(1+\tilde{\delta}_c^2\right)}{\delta_d(1+i\tilde{\delta}_c)}. \tag{B1}$$

In the limit $\tilde{\delta}_c = 0$, E_s can be written in the form $E_s = \frac{-i\sqrt{\alpha}E_{d_0}}{\delta_d}$, where $\sqrt{\alpha}$ characterizes the stimulated field gain. From Eq. (B1) one expects $\alpha = \gamma_\perp^2$.

Equation (B1) explains several features of the measured small-signal gain shown in Fig. 4 of the main text. For $\delta_c = 0$, the stimulated field is in the orthogonal quadrature to the driving field. However, when $\delta_c \neq 0$, as is the case in the data of Fig. 4(b), the response of the cavity to the driving atomic dipole causes the stimulated field to be partially rotated into the same quadrature as the driving field. This rotation breaks the symmetry about $\delta_d = 0$ for both the measured phase and power gain shown in Fig. 4(a).

To quantify the small-signal gain experimentally, we measure the total output power of the laser at the drive frequency for a large range of drive detunings δ_d. We fit the total output power to the gain model shown in Eq. (B2). Equation (B2) is the magnitude squared of Eq. (B1) with the E_{d_0} dependence
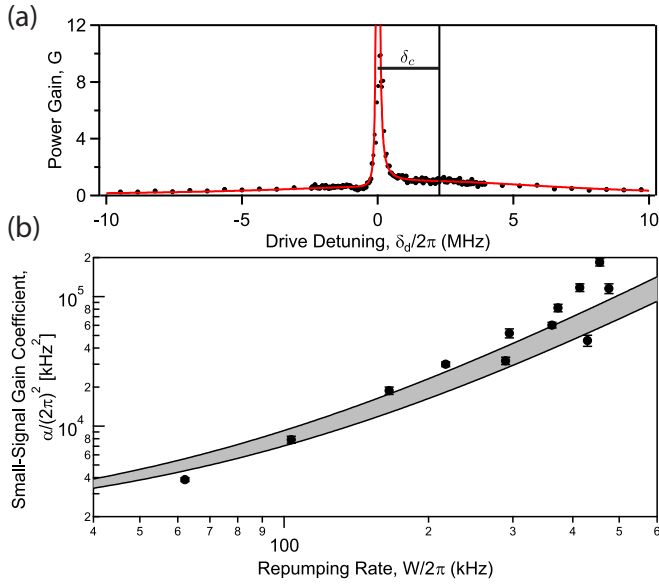
FIG. 5. (Color online) Quantitative small-signal gain measurements. (a) We measure the total transmitted power at the drive frequency ω_d and define power gain G as the measured transmitted power normalized to the drive power transmitted through the cavity on resonance with no atoms present. For these measurements, δ_d is scanned over a frequency range greater than the cavity linewidth κ. The data are fit to the model in Eq. (B2) (red line). Note that here, the cavity resonance marked by the vertical solid line is a few MHz higher than the atomic resonance. (b) From fits to data such as (a), we plot the variation of the fitted gain coefficient α (see text) vs W. The prediction $\alpha = \gamma_\perp^2$ is shown in gray. The width of the gray band corresponds to the uncertainty in an independent calibration of the repumping rate W.

on $\tilde{\delta}_{d,c}$ written explicitly,

$$G(\delta_d, \tilde{\delta}_{d,c}) = \frac{G_0}{1 + \tilde{\delta}_{d,c}^2}$$
$$\times \left\{ 1 - 2\frac{\sqrt{\alpha}(\tilde{\delta}_c - \tilde{\delta}_0)}{(\delta_d - \delta_0)} + \frac{\alpha[1 + (\tilde{\delta}_c - \tilde{\delta}_0)^2]}{(\delta_d - \delta_0)^2} \right\}.$$
(B2)

For a single scan of δ_d, we allow fitting of the parameters G_0, α, δ_c, κ, and δ_0. The fit model constrains the transmitted power to be G_0 when the drive is on resonance with the cavity in the absence of an atomic response. The δ_0 coefficient allows for an arbitrary offset of the atomic transition frequency ω_a from zero. Figure 5(a) displays an example of this measured total output power as a function of δ_d with the fit overlaid in red. In Fig. 5(a), the data have been rescaled such that the fitted coefficient $G_0 = 1$. After this rescaling, the data represent the total power emitted at the drive frequency, normalized to the power transmitted through the cavity when the drive is on resonance with the cavity and no atoms are present. Also, the frequency axis of the data has been adjusted such that $\delta_0 = 0$.

We follow this procedure, measuring the output power and fitting to Eq. (B2), for many repumping rates W. We plot the fitted gain coefficients α versus W in Fig. 5(b). The prediction that $\alpha = \gamma_\perp^2 = (W/2 + \Gamma_D)^2$ is overlaid in gray.
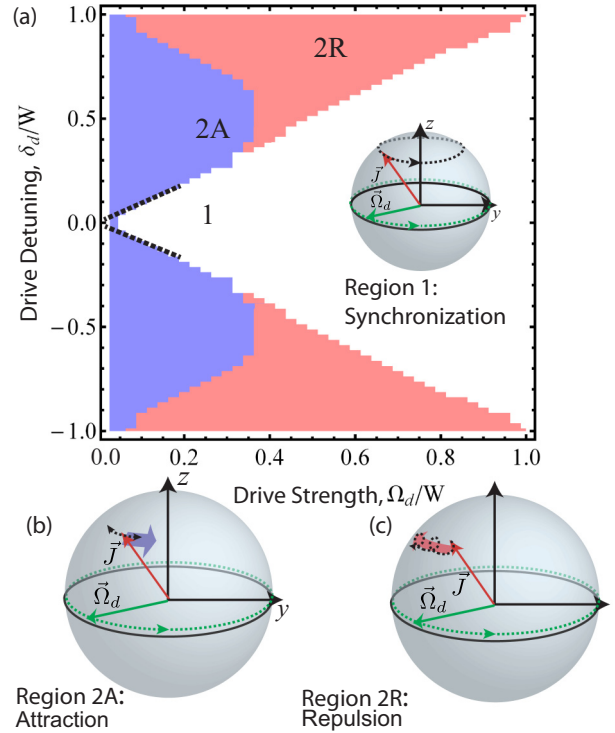

FIG. 6. (Color online) Bloch vector interpretation of the phase diagram. (a) The types of behavior for the driven superradiant laser can be characterized by a phase diagram. The characteristic rates that determine the lasing behavior are drive Rabi frequency Ω_d, detuning δ_d, and repumping rate W. The regions correspond to the number of distinct emission frequencies (1 or 2) and the frequency shift (attraction or repulsion) of the carrier (A and R, respectively). The behavior of the synchronization (a), attraction (b), and repulsion (c) configurations are shown in a Bloch sphere picture. In the frame of the atomic transition frequency ω_a, the drive is represented by a rotation $\vec{\Omega}_d$, with an orientation that rotates along the dashed green trajectory at frequency δ_d. In the unsynchronized case, this modulates the Bloch vector (red vector), causing drift toward or away from the drive, with the average precession of the Bloch vector indicated in each case via the large blue and red arrows. In the synchronized case, the Bloch vector follows the drive all the way around the sphere.

Uncertainty in the prediction (width of the gray band) is due to uncertainty in the experimental calibration of W. The prediction shows reasonable agreement with the theory over a significant range of W.

APPENDIX C: BLOCH VECTOR INTERPRETATION OF PHASE DIAGRAM

The predicted phase diagram is shown in Fig. 6. The behavior in each of the three regions can be visualized by the behavior of the Bloch vector in each regime. In a frame rotating at the atom's natural transition frequency ω_a, the applied drive can be represented by a rotation of the Bloch vector, $\vec{\Omega}_d = \Omega_d[\hat{x}\cos(\delta_d t) + \hat{y}\sin(\delta_d t)]$. $|\Omega_d|$ is the angular frequency of the rotation, and $\hat{\Omega}_d$ is the axis about which the Bloch vector rotates. The azimuthal phase of the applied rotation axis precesses at frequency δ_d. When $\Omega_d \ll |\delta_d|$, the drive acts primarily to slightly modulate the orientation

of the Bloch vector [both Figs. 6(b) and 6(c)]. However, when $\Omega_d > |\delta_d|$, the applied modulation is so large that the Bloch vector can actually follow the drive all the way around the sphere. This is the synchronized region (1) in Fig. 6(a). Near the synchronization transition, the repulsive (2R) versus attractive (2A) behavior is determined by the size of the repumping rate W compared to δ_d and Ω_d.

1. Attractive regime: Mapping to the 2D Van der Pol oscillator

In the case $|\delta_d|, \Omega_d \lesssim W$ (i.e., 2A), the drive does not significantly perturb the laser from its steady-state inversion because any change in J_z caused by the applied field is quickly healed by the repumping process [17]. When J_z is not modified, the azimuthal phase ϕ is partially or fully dragged in the same direction as the rotating axis $\hat{\Omega}_d$ [Fig. 6(a)]. The lasing can be viewed as being captured by the applied drive.

Furthermore, in this regime of weak drive, $|\delta_d|, \Omega_d \lesssim W$, the system can be mapped onto a Van der Pol self-oscillator model with a nonlinear driving term,

$$\dot{j}_- = -i\delta J_- + \lambda J_-(1 - |j_-|^2) + \Omega(1 - \beta|j_-|^2), \quad (C1)$$

with complex amplitude J and characteristic rates λ, δ, Ω, and β. Equation (C1) has an equilibrium amplitude $|j_-|^2 = 1$. The nonlinearity of the applied drive is governed by the parameter β. For $\beta = 0$, this model has been well studied [18,19].

To explicitly show the mapping of the optical Bloch equations [Eq. (A3)] onto this form, we first eliminate the cavity field E by assuming operation in the deep bad-cavity limit, and we assume that J_z is not perturbed by the drive. Setting $\dot{J}_z$ equal to zero gives the nominal steady-state value

$$J_{z_{ss}} = \frac{N}{2} - \frac{C\gamma}{W}|J_-|^2. \quad (C2)$$

One can then insert $J_{z_{ss}}$ into the J_- equation in Eq. (A3), which leads to

$$\dot{J}_- = -i\delta_d J_- + J_- \left[\left(\frac{NC\gamma}{2} - \frac{W}{2} \right) - \frac{(C\gamma)^2}{W}|J_-|^2 \right]$$
$$+ \frac{\Omega_d}{2} \left(\frac{N}{2} - \frac{C\gamma}{W}|J_-|^2 \right). \quad (C3)$$

For the case of optimal repumping, we set $W = W_{opt} = \frac{NC\gamma}{2}$, and we normalize J_- to its steady-state value defining $j_- = J_-/J_{-_{ss}}$, where $J_{-_{ss}} = \frac{N}{\sqrt{8}}$, giving

$$\dot{j}_- = -i\delta_d j_- + \frac{NC\gamma}{4}(1 - |j_-|^2) + \frac{\Omega_d}{\sqrt{2}} \left(1 - \frac{|j_-|^2}{2} \right). \quad (C4)$$

This equation is of the same form as Eq. (C1) with $\delta = \delta_d$, $\Omega = \frac{\Omega_d}{\sqrt{2}}$, $\beta = \frac{1}{2}$, and $\lambda = \frac{NC\gamma}{4}$. We can define an effective drive strength $\Omega'_d = \frac{\Omega_d}{\sqrt{2}}(1 - \frac{|j_-|^2}{2})$. For a weak drive, the laser remains close to its steady state. One finds $\Omega'_d = \frac{1}{\sqrt{8}}\Omega_d$, and the system can be thought of as behaving similarly to the standard driven Van der Pol oscillator of Refs. [18,19] with a constant driving term.

2. Repulsive regime: 3D dynamics

When the drive is applied with a large detuning $|\delta_d| \gtrsim W$ [i.e., (2R)], the repumping at rate W cannot heal the changes in the inversion J_z caused by the applied drive [17]. J_z can no longer be considered static and thus introduces a third degree of freedom (in addition to J_x and J_y) in the system. In this regime, the Van der Pol model breaks down, and small oscillations in J_z must be taken into account. The unhealed modulations of J_z at frequency δ_d coherently interact with the applied rotation due to the drive to cause the Bloch vector to acquire on average a small precession in the opposite sense to the precession of the drive rotation axis $\hat{\Omega}_d$ [shown in Fig. 6(c)]. The precession rate is second order in Ω_d and can be identified as an ac Stark shift that leads to the observed frequency repulsion in region (2R). To emphasize, this shift does not appear in region (2A) because there the repumping process acts to smooth out the modulations in J_z that are essential for creating the ac Stark shift.

The ac Stark shift can be derived to leading order by perturbatively allowing for small oscillations in J_z. In this way, we can mathematically show the additional repulsive behavior not evident in the two-dimensional model of Eq. (C1). The optical Bloch equation for J_z allowing for modulation, and written in the frame of the drive frequency ω_d, is

$$\dot{J}_z = -W J_z + \frac{N}{2} W - C\gamma|J_-|^2 - \Omega_d \text{Re}(J_-). \quad (C5)$$

We treat this equation perturbatively by assuming that J_- primarily oscillates at the self-lasing frequency. From this we can derive a leading-order repulsion term giving a new self-lasing frequency,

$$\delta' = \delta_d + \frac{\Omega_d^2 \delta_d}{2(\delta_d^2 + W^2)}, \quad (C6)$$

which arises from oscillations in J_z coupling into an average frequency repulsion of the Bloch vector. This repulsive physics is not present in the driven Van der Pol oscillator and arises from the Bloch vector occupying a higher, three-dimensional parameter space.

[1] J. G. Bohnet, Z. Chen, J. M. Weiner, D. Meiser, M. J. Holland, and J. K. Thompson, Nature (London) **484**, 78 (2012).

[2] J. G. Bohnet, Z. Chen, J. M. Weiner, K. C. Cox, and J. K. Thompson, Phys. Rev. A **88**, 013826 (2013).

[3] J. M. Weiner, K. C. Cox, J. G. Bohnet, Z. Chen, and J. K. Thompson, Appl. Phys. Lett. **101**, 261107 (2012).

[4] D. Meiser, J. Ye, D. R. Carlson, and M. J. Holland, Phys. Rev. Lett. **102**, 163601 (2009).

[5] S. Inouye, A. P. Chikkatur, D. M. Stamper-Kurn, J. Stenger, D. E. Pritchard, and W. Ketterle, Science **285**, 571 (1999).

[6] A. T. Black, H. W. Chan, and V. Vuletić, Phys. Rev. Lett. **91**, 203001 (2003).

[7] S. Slama, S. Bux, G. Krenz, C. Zimmermann, and P. W. Courteille, Phys. Rev. Lett. **98**, 053603 (2007).

[8] J. A. Greenberg, B. L. Schmittberger, and D. J. Gauthier, Opt. Express **19**, 022535 (2011).

[9] K. Baumann, C. Guerlin, F. Brennecke, and T. Esslinger, Nature (London) **464**, 1301 (2010).

[10] E. G. D. Torre, S. Diehl, M. D. Lukin, S. Sachdev, and P. Strack, Phys. Rev. A **87**, 023831 (2013).

[11] S. Gopalakrishnan, B. L. Lev, and P. M. Goldbart, Phys. Rev. Lett. **107**, 277201 (2011).

[12] P. Strack and S. Sachdev, Phys. Rev. Lett. **107**, 277202 (2011).

[13] S. Gopalakrishnan, B. L. Lev, and P. M. Goldbart, Philos. Mag. **92**, 353 (2012).

[14] M. Xu, D. A. Tieri, E. C. Fine, J. K. Thompson, and M. J. Holland, Phys. Rev. Lett. **113**, 154101 (2014).

[15] G. Manzano, F. Galve, G. L. Giorgi, E. Hernández-García, and R. Zambrini, Sci. Rep. **3**, 1439 (2013).

[16] S. Walter, A. Nunnenkamp, and C. Bruder, Phys. Rev. Lett. **112**, 094102 (2014).

[17] J. G. Bohnet, Z. Chen, J. M. Weiner, K. C. Cox, and J. K. Thompson, Phys. Rev. Lett. **109**, 253602 (2012).

[18] A. Pikovsky, M. Rosenblum, and J. Kurths, Int. J. Bifurcation Chaos **10**, 2291 (2000).

[19] A. Pikovsky, M. Rosenblum, and J. Kurths, *Synchronization: A Universal Concept in Nonlinear Sciences* (Cambridge University Press, Cambridge, 2003).

[20] A. E. Siegman, in *Lasers*, edited by A. Kelly (University Science Books, Mill Valley, California, 1986).

[21] R. Lang, IEEE J. Quantum Electron. **18**, 976 (1982).

[22] F. Mogensen, H. Olesen, and G. Jacobsen, IEEE J. Quantum Electron. **21**, 784 (1985).

[23] T. Simpson, J. Liu, K. Huang, and K. Tai, Quantum Semiclassical Opt.: J. Eur. Opt. Soc. B **9**, 765 (1997).

[24] G. L. Oppo, A. Politi, G. L. Lippi, and F. T. Arecchi, Phys. Rev. A **34**, 4000 (1986).

[25] W. Li, N. H. Zhu, L. X. Wang, J. H. Ke, S. F. Chen, X. Q. Qi, B. H. Zhang, and L. Xie, IEEE J. Quantum Electron. **46**, 796 (2010).

[26] J. G. Bohnet, Z. Chen, J. M. Weiner, K. C. Cox, D. Meiser, M. J. Holland, and J. K. Thompson, EPJ Web Conf. **57**, 03003 (2013).

[27] D. Meiser and M. J. Holland, Phys. Rev. A **81**, 033847 (2010).

[28] J. G. Bohnet, Z. Chen, J. M. Weiner, K. C. Cox, and J. K. Thompson, Phys. Rev. A **89**, 013806 (2014).

[29] V. DeGiorgio and M. O. Scully, Phys. Rev. A **2**, 1170 (1970).

[30] M. J. Martin, D. Meiser, J. W. Thomsen, J. Ye, and M. J. Holland, Phys. Rev. A **84**, 063813 (2011).